

Circular dichroism induction in WS_2 by a chiral plasmonic metasurface

FERNANDO LORÉN,^{1,2} CYRIAQUE GENET,³ AND LUIS MARTIN-MORENO^{1,2,*}

¹*Instituto de Nanociencia y Materiales de Aragón (INMA), CSIC-Universidad de Zaragoza, 50009 Zaragoza*

²*Departamento de Física de la Materia Condensada, Universidad de Zaragoza, 50009 Zaragoza*

³*University of Strasbourg and CNRS, CESQ & ISIS (UMR 7006), 8, allée G. Monge, 67000 Strasbourg, France*

**lmm@unizar.es*

Abstract: We investigate the interaction between a monolayer of WS_2 and a chiral plasmonic metasurface. WS_2 possesses valley excitons that selectively couple with one-handed circularly polarised light. At the same time, the chiral plasmonic metasurface exhibits spin-momentum locking, leading to a robust polarisation response in the far field. Using a scattering formalism based on the coupled mode method, we analyse various optical properties of the WS_2 monolayer. Specifically, we demonstrate the generation of circular dichroism in the transition metal dichalcogenide (TMD) by harnessing the excitation of surface plasmon polaritons (SPPs) in the metasurface. Moreover, we observe the emergence of other guided modes, opening up exciting possibilities for further exploration in TMD-based devices.

1. Introduction

Transition metal dichalcogenides (TMDs), such as MoS_2 , WS_2 , and MoSe_2 , have garnered significant attention due to their unique electronic, optical, and mechanical properties [1–7]. TMDs consist of atomically thin layers held together by weak van der Waals forces. The monolayers of these materials exhibit fascinating characteristics that make them highly desirable for a range of applications [8, 9], including electronics [10], optoelectronics [11, 12], energy storage [13] and sensing [14]. Furthermore, circularly polarised light is particularly relevant in this context, as it enables the selective excitation and manipulation of the characteristic valley excitons of the TMDs [15–17].

On the other hand, plasmonic metasurfaces have demonstrated a wide range of applications [18–20] such as sensing [21] or imaging [22, 23]. Chiral structures, in particular, have emerged due to their capacity to manipulate and control the polarisation of light waves [24–30]. Furthermore, they can exhibit spin-momentum locking (SML), which refers to the coupling between the polarisation and momentum of the light waves involved [31]. The SML of the metasurface enables a particularly compelling application in the field of valleytronics [32–37], where the spin angular momentum of emitted light can be used to excite and detect valley excitons selectively.

Although the valley-selective circular dichroism has already been reported in TMDs [38], there is no proof of circular dichroism (CD) in this system yet. In this work, as proof of concept, we study the system composed of a WS_2 monolayer over a chiral plasmonic metasurface to analyse the CD induced in the WS_2 . Finally, we show that guided modes can enhance the CD in the presence of a dielectric spacer between the TMD and the metasurface. Unlike SPPs, these modes have a transverse electric (TE) field, but we observe that, mutatis mutandis, its excitation satisfies the 3-step model derived in [39].

2. Theoretical description

We consider a WS_2 monolayer deposited over a chiral plasmonic metasurface, with a dielectric spacer in between (see Figure 1(a)), which is based on [32]. As in the experiments in Ref. [32],

the metasurface is characterised by a periodic array of $N = 6$ rectangular dimples step-wisely rotated with a winding number of $n_w = 1/2$, which is the number of complete 2π rotations along the whole unit cell. The unit cell (see Fig. 1(b)) is periodically repeated in both \vec{u}_x and \vec{u}_y directions.

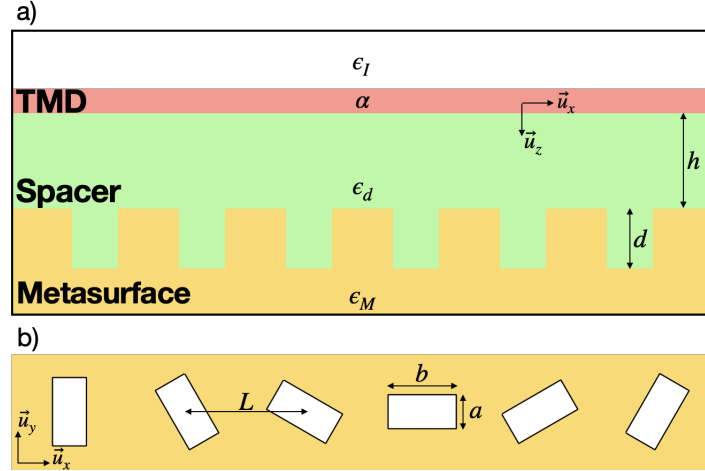


Fig. 1. a) Scheme of the system studied in the article, with the corresponding defining magnitudes. b) Unit cell with $N = 6$ and $n_w = 1/2$. Based on [32].

We use the coupled-mode method (CMM) to derive the system's electromagnetic (EM) fields. This method has been extensively employed to study EM properties in plasmonic arrays [39–42]. The CMM expands the EM fields in plane waves in the free space regions and waveguide modes inside the dimples and finds the electric field amplitudes by properly matching the EM fields at the interfaces. The excitation of our system consists of an electromagnetic plane wave impinging our metasurface with an in-plane wavevector $\vec{k}^{in} = k_x^{in}\vec{u}_x + k_y^{in}\vec{u}_y$ and an incident polarisation σ^{in} . The goal is to compute the coefficients associated with the Bragg orders, which define the EM fields in the different regions.

We do not present the full equations resulting from the CMM method, as they have been given in a similar structure without the TMD in [39]. The effect of the 2D material is straightforwardly included by considering an additional interface and satisfying the in-plane magnetic field discontinuity that arises due to the conductivity α .

The accuracy of the CMM relies on the number of considered Bragg modes in the simulations. In our particular case, we have considered 21 modes in the \vec{u}_x direction and 3 modes in the \vec{u}_y direction, being $\vec{G}_x = 2\pi/(6L)\vec{u}_x$ and $\vec{G}_y = 2\pi/L\vec{u}_y$ the reciprocal lattice or Bragg vectors of the unit cell. We have checked that adding more Bragg modes introduces less than 1% variation in the obtained results.

We treat the metallic structure using the surface impedance boundary conditions (SIBC) approximation, which considers the actual dielectric constant of the metal ϵ_M and the penetration of the EM fields into the metal slab through the surface impedance $z_s = 1/\sqrt{\epsilon_M + 1}$, which leads to the exact dispersion relation of SPPs in a metal-vacuum interface. The semi-infinite region above the 2D material and the dielectric spacer is characterised by the dielectric constants ϵ_I and ϵ_d , respectively. Finally, the 2D material is characterised by its 2D conductivity α . We obtain it from the experimental dielectric constant ϵ_{2D} [43] through $\alpha = w\pi(\epsilon_{2D} - 1)/(\lambda i)$, where w is the width of the 2D material ($w \approx 1\text{ nm}$), λ is the wavelength of the EM fields and Gaussian units have been used. Moreover, we fit the conductivity to remove the background, which is associated with sample imperfections and can be decreased by, for instance, encapsulating the

TMD between graphene monolayers [44, 45].

Once the EM fields are computed, we obtain the total absorptance of the system as $A_T = (W_{inc} - W_{ref})/W_{inc}$, where W_{inc} and W_{ref} are the incoming and reflected EM energy fluxes, respectively, calculated via the integration of the Poynting vector over an $x - y$ plane in the semi-infinite regions above the 2D material. The reflectance is $R = W_{ref}/W_{inc} = 1 - A_T$. The absorptance of the WS_2 monolayer depends on the conductivity tensor $\overleftrightarrow{\alpha}$ and the in-plane electric field \vec{E} at the 2D material, integrated over the $x - y$ plane: $A_{WS_2} = (\int \vec{j}^* \vec{E} dx dy) / W_{inc} = (\int \vec{E}^* \overleftrightarrow{\alpha} \vec{E} dx dy) / W_{inc}$. In the linear polarisation basis $\overleftrightarrow{\alpha}$ is diagonal, with diagonal components equal to α .

Associated with them, we also analyse the circular dichroism and the g-factor: $CD = A_{WS_2}^+ - A_{WS_2}^-$, $CD_{norm} = CD / (A_{WS_2}^+ + A_{WS_2}^-)$, $g = R^+ - R^-$, and $g_{norm} = g / (R^+ + R^-)$. The superscripts refer to the spin of the incoming plane waves $\sigma^{in} = \pm$, and we will work with both normalised and not-normalized magnitudes.

For definiteness, the geometrical parameters considered in this paper are as in Ref. [32]: each dimple has a short side $a = 80\text{ nm}$, a long side $b = 220\text{ nm}$ and a depth $d = 60\text{ nm}$, and the distance between the centres of nearest dimples is $L = 480\text{ nm}$ (in both \vec{u}_x and \vec{u}_y).

3. Circular Dichroism in WS_2

To analyse the quantities described in the previous section, we range both the energy ω and the momentum k_x^{in} of the incoming plane wave.

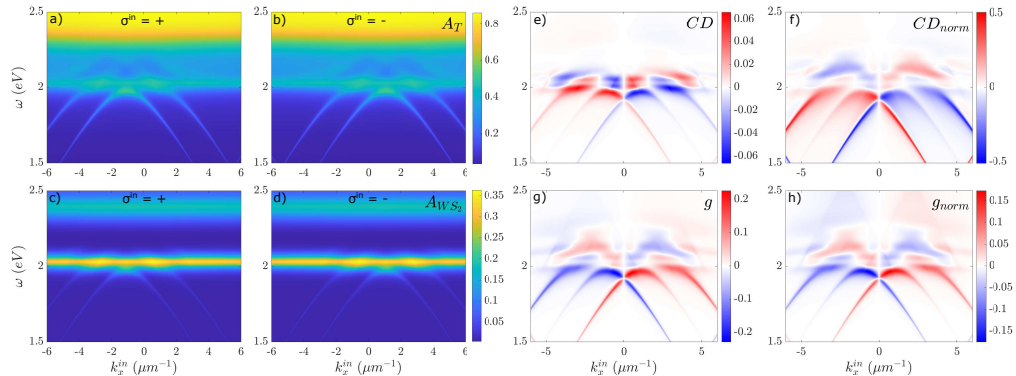


Fig. 2. (a,b) Total absorptance of the system for $\sigma^{in} = \pm$, respectively. (c,d) Absorptance of the WS_2 monolayer for $\sigma^{in} = \pm$, respectively. (e) Circular dichroism. (f) Normalised circular dichroism. (g) g-factor. (h) Normalised g-factor. For all the plots, we have considered a distance $h = 10\text{ nm}$ between the metasurface and the WS_2 , above the 2D material $\epsilon_I = 1$ (vacuum), and a spacer dielectric constant $\epsilon_d = 2.5$, which corresponds to the typical SiO_2 spacer.

In Figs. 2(a-d), we observe the well-known behaviour of both the metasurface and the TMD monolayer. In the upper region of the A_T^\pm figures, we identify the large absorption of gold at $\lambda \sim 500\text{ nm}$. Moreover, the four absorptance figures present plasmonic parabolic features provided by the metasurface. The SML, produced by the rotation of the dimples along the unit cell, is also noted through the selective excitation of the left and right SPPs (which depend on the spin $\sigma^{in} = \pm$ of the incoming plane wave, respectively [32, 39]). The influence of the WS_2 monolayer is also seen in all absorptance figures. Both exciton bands are apparent: The A-exciton band appears at $\omega \simeq 2.03\text{ eV}$, and the B-exciton band at $\omega \simeq 2.4\text{ eV}$. Besides, in Figs. 2(c,d), we observe the interplay between the A-exciton band from the WS_2 monolayer and the SPP through the absorptance enhancement at the band's crossing points.

The same metasurface was previously studied in [39], where it was shown that *spin-momentum locking* is an approximate symmetry. The symmetry breakdown arises because the EM plane waves are transversal with respect to their momentum, while the interaction with the surface presents symmetries with respect to the metasurface normal. Consequently, when circularly polarised light is projected onto the planar surface, it transforms into an elliptical polarisation state comprising a combination of \pm spin states, spoiling the SML effect. This is not apparent in the contour plots in Fig. 2 because of their limited resolution. However, if we cut Fig. 2(a) at fixed energy, we would observe two small absorptance peaks at the k_x^{in} for which plasmon with the opposite spin states appear.

Figs. 2(e,f) show the computed CD and the CD_{norm} . We observe a different absorptance in the WS_2 depending on the incident spin σ^{in} . Notice that, without the chiral metasurface, the K valley would preferentially absorb + light (in fact, it would only absorb + light at normal incidence) and the same for the K' valley with respect to + light, but this would lead to $CD = 0$. The non-zero CD in the TMD monolayer induced by the chiral plasmonic array is maximal when the spin-momentum locked SPPs are excited. In Fig. 2(e), around the A-exciton band, we observe a difference in absorptances of ~ 0.06 , which is large considering that the typical absorptance in that band is ~ 0.3 . Besides, in Fig. 2(f), the plasmonic parabolas present $|CD_{norm}| \simeq 0.5$, which implies that the WS_2 absorptance for one polarization is three times larger than for the opposite.

In Figs. 2(g,h), we represent g and g_{norm} . Their behaviour is inverse to those of CD or A_T^\pm because they are associated with the reflectance R^\pm . For example, g_{norm} at the rightmost parabola is positive because the chiral metasurface reflects the + light while - light excites an SPP and is thus partially absorbed. In general, g_{norm} is mainly determined by the chiral plasmonic metasurface, not being strongly affected by the presence of the TMD.

These results are just a proof of concept of how CD in a 2D material can be induced by a chiral plasmonic array. Optimising the structure's geometric parameters to enhance the circular dichroism or other quantities is straightforward, given the model's simplicity. For example, we could explore varying the distance between the dimples, their size and depth, the distance between the metasurface and the 2D material, or the dielectric constant of the spacer, among other parameters.

4. Influence of the TE waveguide modes

The second main result of this article is developed in this section, where we show that the spacer can induce the existence of a set of guided modes with imprinted chiral properties from the chiral holey surface.

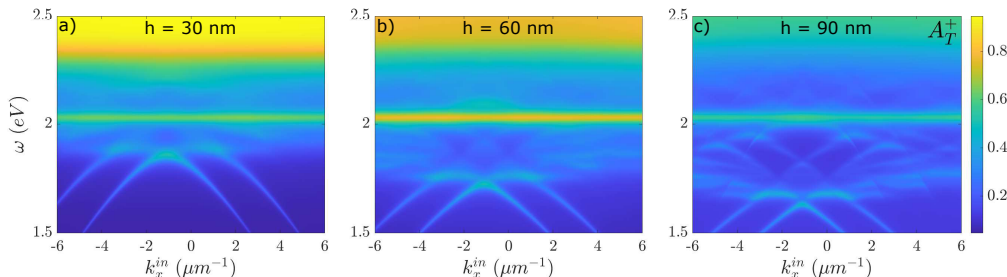


Fig. 3. Total absorptance, considering $\epsilon_I = 1$, $\epsilon_d = 2.5$ and $\sigma^{in} = +$. For different distances from the metasurface to the WS_2 monolayer: (a) $h = 30\text{ nm}$, (b) $h = 60\text{ nm}$, and (c) $h = 90\text{ nm}$.

In Fig. 3, we represent A_T^+ for three different distances between the metasurface and the WS_2 monolayer, h . The SPPs parabolic branches are excited at lower incident energies as h increases.

At the same time, we observe the appearance of new parabolas for larger h . These are the emerging guided modes.

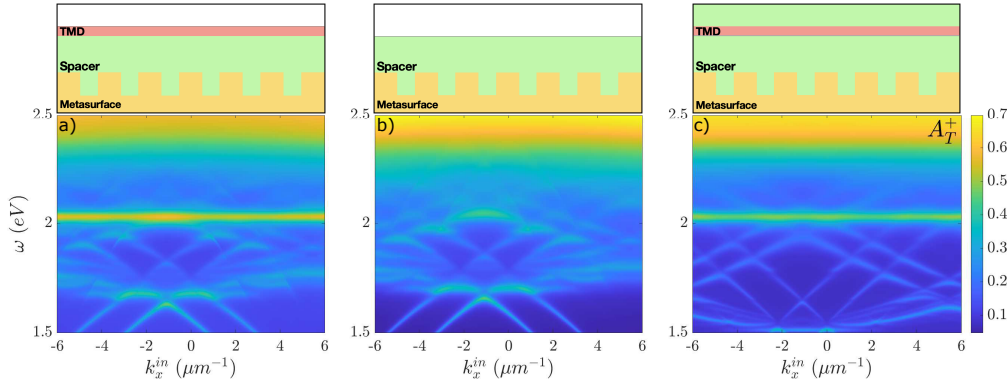


Fig. 4. Total absorptance, considering $\epsilon_I = 1$, $\epsilon_d = 2.5$, $h = 90\text{ nm}$ and $\sigma^{in} = +$. For the different structures above each contour plot: (a) With the WS_2 monolayer (same as Fig. 3(c)), (b) Without the WS_2 monolayer, and (c) With the WS_2 monolayer and $\epsilon_I = 2.5$.

In order to understand the origin of these guided modes, Fig. 4 renders A_T^+ for three different situations, sketched above the plots. Fig. 4(a) is the same as Fig. 3(c). Fig. 4(b) is computed by removing the WS_2 from the top of the dielectric spacer. Fig. 4(c) considers the TMD, but with the region above the WS_2 also having dielectric constant $\epsilon_I = 2.5$. These modes already appear in Fig. 4(b), when no WS_2 monolayer is present. Besides, only the SPPs are excited if the semi-infinite superstrate is considered to have the same dielectric constant of the spacer, even if we consider the presence of the WS_2 layer. Thus, the guided modes are due to the presence of the spacer and not to the TMD (although the 2D material slightly affects the required energy for their excitation).

These spacer-induced guided modes are TE-polarised. To show how this changes the polarisation response of the considered structure, we represent in Fig. 5 the total absorptance of the system A_T for four incident polarisations. Figs. 5(a,b) also show that the SML holds for the guided modes. However, for linearly polarised light with $\sigma^{in} = TM$ (see Fig. 5(c)), absorptance is enhanced at the central plasmonic parabola but vanishes for the guided mode. Complementarily, for $\sigma^{in} = TE$ (see Fig. 5(d)), we observe just the opposite: an enhancement for the central parabola of the guided mode and a substantial reduction for the corresponding SPP.

Note that the modified SML rules, developed in [39] to address the resonant excitation of plasmons, also apply to these guided modes when slightly modified to incorporate their TE nature properly. Scattering under resonant excitation can be understood as a three-step scattering process. First, the incoming plane wave picks up grating momentum to excite the SPP/guided mode, ending with polarisation dictated by the SML rules. In the second step, this polarisation is projected onto TM/TE polarisation states due to the linear polarization of the confined modes. Lastly, the SPP/guided mode outcouples via another SML process. Both in- and out-coupling processes can be “normal” (maintaining the polarisation) or “chiral” (which reduces or increases the plane wave spin when the geometric momentum k_g , associated with the rotation of the dimples, is added or subtracted).

To conclude, in Fig. 6, we represent the CD and CD_{norm} considering $h = 90\text{ nm}$, $\epsilon_I = 1$ and $\epsilon_d = 2.5$. The TE-guided modes also induce circular dichroism in the WS_2 monolayer. We notice that $|CD| \simeq 0.04$ around the A-exciton band and $|CD_{norm}| \simeq 0.3$ when we excite one of these modes. These magnitudes are not as large as those Figs. 2(e,f) but demonstrate inducing chiral

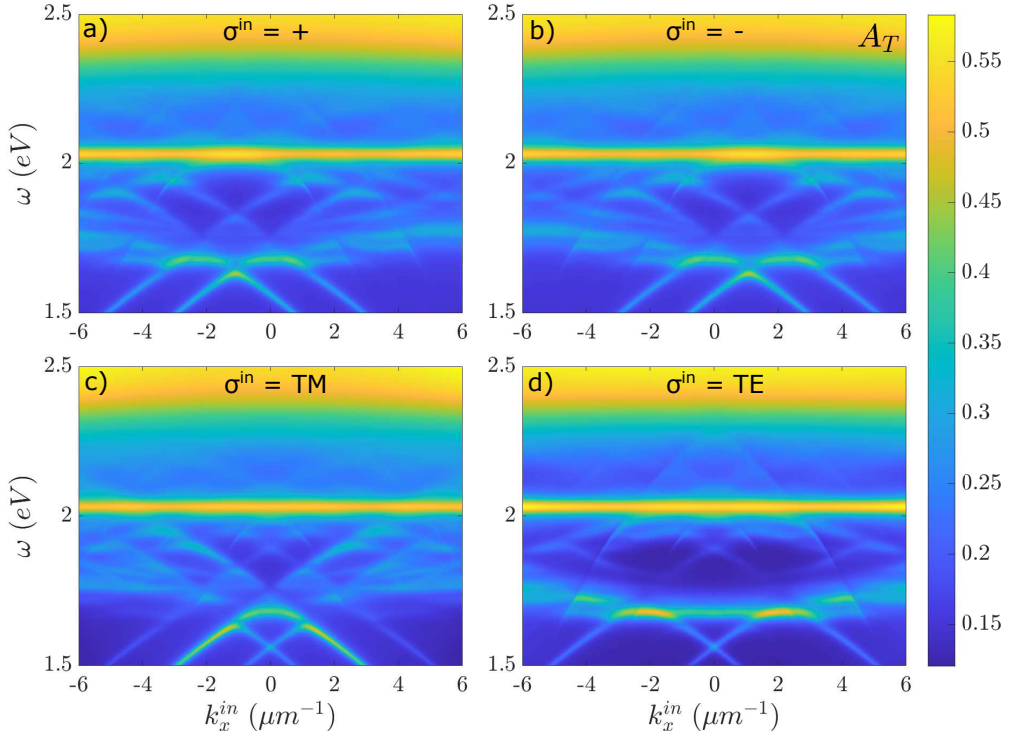


Fig. 5. Total absorptance, considering $h = 90\text{ nm}$ and $\epsilon_d = 2.5$. For incident polarization: (a) $\sigma^{in} = +$, (b) $\sigma^{in} = -$, (c) $\sigma^{in} = p \equiv TM$, and (d) $\sigma^{in} = s \equiv TE$.

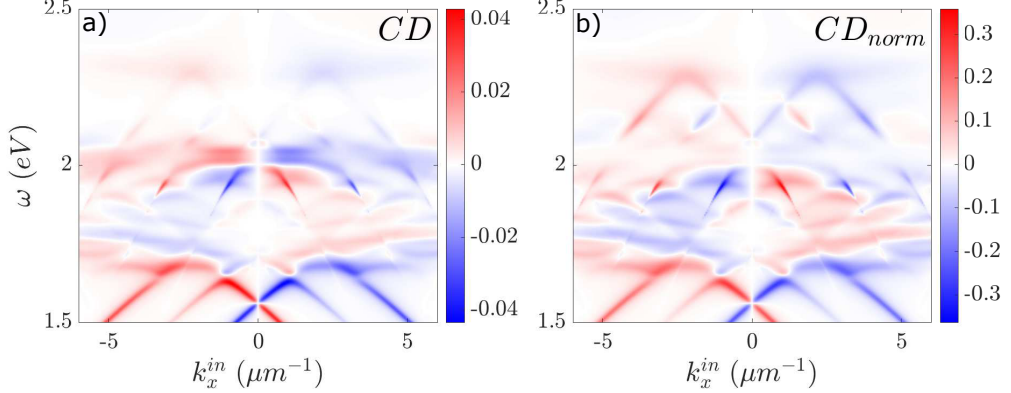


Fig. 6. (a) Circular dichroism. (b) Normalised circular dichroism. We have considered $h = 90\text{ nm}$ and $\epsilon_d = 2.5$.

behaviour in the WS_2 monolayer through the TE-guided modes, and the possibility to use the spacer layer to enhance this phenomenon further.

5. Conclusion

We have presented a way to obtain circular dichroism in transition metal dichalcogenides using chiral plasmonic metasurfaces. Additionally, a transverse electric waveguide mode has been observed and demonstrated to cause CD in TMDs. This work is a proof of concept in a

non-optimized structure; CD values are expected to be substantially higher after optimisation over the whole range of parameters. In particular, after optimisation, the transverse electric character of the guided modes is expected to couple them better than SPPs to the TMDs.

Our characterisation of the 2D material is simple, only based on its permittivity tensor. By changing this tensor into the circularly polarised basis, we can easily split the full TMD optical behaviour into the K and K' valleys components. This allows us to study the different valley phenomena with our simple formalism. However, magnitudes such as the valley contrast or the valley-selective circular dichroism would still require considering the inter-valley scattering to embrace the exciton dynamics, which has been proved to be essential in the analysis of TMDs [32, 46, 47].

The findings presented here pave the way for further exploration in the field of chiral optics and valleytronics. Indeed, the induced circular dichroism in TMDs may have applications in areas such as chiral sensing, imaging, and quantum information processing [6, 15, 48–51].

Funding. We acknowledge Project PID2020-115221GB-C41 was financed by MCIN/AEI/10.13039/501100011033 and the Aragon Government through Project Q-MAD.

This work is part of the Interdisciplinary Thematic Institute QMat of the University of Strasbourg, CNRS, and Inserm. It was supported by the following programs: IdEx Unistra (ANR-10-IDEX-0002), SFRI STRATUS project (ANR-20-SFRI-0012), and USIAS (ANR-10-IDEX-0002-02), under the framework of the French Investments for the Future Program.

Acknowledgments. FL and LMM also acknowledge the Aragón government project Q-MAD.

Disclosures. The authors have no conflicts to disclose.

Data Availability Statement. Data underlying the results presented in this paper are not publicly available but may be obtained from the authors upon reasonable request.

References

1. Q. H. Wang, K. Kalantar-Zadeh, A. Kis, J. N. Coleman, and M. S. Strano, “Electronics and optoelectronics of two-dimensional transition metal dichalcogenides,” *Nat. Nanotechnol.* **7**, 699–712 (2012).
2. B. W. H. Baugher, H. O. H. Churchill, Y. Yang, and P. Jarillo-Herrero, “Optoelectronic devices based on electrically tunable p–n diodes in a monolayer dichalcogenide,” *Nat. Nanotechnol.* **9**, 262–267 (2014).
3. Q. Zhang, S. A. Yang, W. Mi, Y. Cheng, and U. Schwingenschlögl, “Large spin-valley polarization in monolayer MoTe₂ on top of EuO(111),” *Adv. Mater.* **28**, 959–966 (2015).
4. M. Eginligil, B. Cao, Z. Wang, X. Shen, C. Cong, J. Shang, C. Soci, and T. Yu, “Dichroic spin–valley photocurrent in monolayer molybdenum disulphide,” *Nat. Commun.* **6** (2015).
5. S. Manzeli, D. Ovchinnikov, D. Pasquier, O. V. Yazyev, and A. Kis, “2d transition metal dichalcogenides,” *Nat. Rev. Mater.* **2** (2017).
6. H.-K. Li, K. Y. Fong, H. Zhu, Q. Li, S. Wang, S. Yang, Y. Wang, and X. Zhang, “Valley optomechanics in a monolayer semiconductor,” *Nat. Photonics* **13**, 397–401 (2019).
7. L. Li, L. Shao, X. Liu, A. Gao, H. Wang, B. Zheng, G. Hou, K. Shehzad, L. Yu, F. Miao, Y. Shi, Y. Xu, and X. Wang, “Room-temperature valleytronic transistor,” *Nat. Nanotechnol.* **15**, 743–749 (2020).
8. K. F. Mak, C. Lee, J. Hone, J. Shan, and T. F. Heinz, “Atomically thin MoS₂: A new direct-gap semiconductor,” *Phys. Rev. Lett.* **105** (2010).
9. Y.-Q. Bie, G. Grosso, M. Heuck, M. M. Furchi, Y. Cao, J. Zheng, D. Bunandar, E. Navarro-Moratalla, L. Zhou, D. K. Efetov, T. Taniguchi, K. Watanabe, J. Kong, D. Englund, and P. Jarillo-Herrero, “A MoTe₂-based light-emitting diode and photodetector for silicon photonic integrated circuits,” *Nat. Nanotechnol.* **12**, 1124–1129 (2017).
10. K. F. Mak, K. L. McGill, J. Park, and P. L. McEuen, “The valley hall effect in MoS₂ transistors,” *Science* **344**, 1489–1492 (2014).
11. W. Yang, J. Shang, J. Wang, X. Shen, B. Cao, N. Peimyoo, C. Zou, Y. Chen, Y. Wang, C. Cong, W. Huang, and T. Yu, “Electrically tunable valley-light emitting diode (vLED) based on CVD-grown monolayer WS₂,” *Nano Lett.* **16**, 1560–1567 (2016).
12. Y. Wan, J. Xiao, J. Li, X. Fang, K. Zhang, L. Fu, P. Li, Z. Song, H. Zhang, Y. Wang, M. Zhao, J. Lu, N. Tang, G. Ran, X. Zhang, Y. Ye, and L. Dai, “Epitaxial single-layer MoS₂ on GaN with enhanced valley helicity,” *Adv. Mater.* **30**, 1703888 (2017).
13. M. Bernardi, M. Palummo, and J. C. Grossman, “Extraordinary sunlight absorption and one nanometer thick photovoltaics using two-dimensional monolayer materials,” *Nano Lett.* **13**, 3664–3670 (2013).
14. E. Lee, Y. S. Yoon, and D.-J. Kim, “Two-dimensional transition metal dichalcogenides and metal oxide hybrids for gas sensing,” *ACS Sensors* **3**, 2045–2060 (2018).

15. J. R. Schaibley, H. Yu, G. Clark, P. Rivera, J. S. Ross, K. L. Seyler, W. Yao, and X. Xu, "Valleytronics in 2d materials," *Nat. Rev. Mater.* **1** (2016).
16. K. M. McCreary, M. Currie, A. T. Hanbicki, H.-J. Chuang, and B. T. Jonker, "Understanding variations in circularly polarized photoluminescence in monolayer transition metal dichalcogenides," *ACS Nano* **11**, 7988–7994 (2017).
17. S.-H. Gong, F. Alpegiani, B. Sciacca, E. C. Garnett, and L. Kuipers, "Nanoscale chiral valley-photon interface through optical spin-orbit coupling," *Science* **359**, 443–447 (2018).
18. H.-T. Chen, A. J. Taylor, and N. Yu, "A review of metasurfaces: physics and applications," *Reports on Prog. Phys.* **79**, 076401 (2016).
19. S. G. Rodrigo, F. de León-Pérez, and L. Martín-Moreno, "Extraordinary optical transmission: Fundamentals and applications," *Proc. IEEE* **104**, 2288–2306 (2016).
20. P. Genevet, F. Capasso, F. Aieta, M. Khorasaninejad, and R. Devlin, "Recent advances in planar optics: from plasmonic to dielectric metasurfaces," *Optica* **4**, 139 (2017).
21. M. Beruete and I. Jáuregui-López, "Terahertz sensing based on metasurfaces," *Adv. Opt. Mater.* **8**, 1900721 (2019).
22. C. M. Watts, D. Shrekenhamer, J. Montoya, G. Lipworth, J. Hunt, T. Sleasman, S. Krishna, D. R. Smith, and W. J. Padilla, "Terahertz compressive imaging with metamaterial spatial light modulators," *Nat. Photonics* **8**, 605–609 (2014).
23. F. Walter, G. Li, C. Meier, S. Zhang, and T. Zentgraf, "Ultrathin nonlinear metasurface for optical image encoding," *Nano Lett.* **17**, 3171–3175 (2017).
24. Z. Bomzon, G. Biener, V. Kleiner, and E. Hasman, "Space-variant pancharatnam–berry phase optical elements with computer-generated subwavelength gratings," *Opt. Lett.* **27**, 1141 (2002).
25. Y. Zhao and A. Alù, "Manipulating light polarization with ultrathin plasmonic metasurfaces," *Phys. Rev. B* **84** (2011).
26. N. Yu, F. Aieta, P. Genevet, M. A. Kats, Z. Gaburro, and F. Capasso, "A broadband, background-free quarter-wave plate based on plasmonic metasurfaces," *Nano Lett.* **12**, 6328–6333 (2012).
27. N. Shitrit, I. Yulevich, E. Maguid, D. Ozeri, D. Veksler, V. Kleiner, and E. Hasman, "Spin-optical metamaterial route to spin-controlled photonics," *Science* **340**, 724–726 (2013).
28. L. Langguth, A. H. Schokker, K. Guo, and A. F. Koenderink, "Plasmonic phase-gradient metasurface for spontaneous emission control," *Phys. Rev. B* **92** (2015).
29. M. Cotrufo, C. I. Osorio, and A. F. Koenderink, "Spin-dependent emission from arrays of planar chiral nanoantennas due to lattice and localized plasmon resonances," *ACS Nano* **10**, 3389–3397 (2016).
30. C. Yan, X. Wang, T. V. Raziman, and O. J. F. Martin, "Twisting fluorescence through extrinsic chiral antennas," *Nano Lett.* **17**, 2265–2272 (2017).
31. K. Y. Bliokh, F. J. Rodríguez-Fortuño, F. Nori, and A. V. Zayats, "Spin–orbit interactions of light," *Nat. Photonics* **9**, 796–808 (2015).
32. T. Chervy, S. Azzini, E. Lorchat, S. Wang, Y. Gorodetski, J. A. Hutchison, S. Berciaud, T. W. Ebbesen, and C. Genet, "Room temperature chiral coupling of valley excitons with spin-momentum locked surface plasmons," *ACS Photonics* **5**, 1281–1287 (2018).
33. Z. Li, C. Liu, X. Rong, Y. Luo, H. Cheng, L. Zheng, F. Lin, B. Shen, Y. Gong, S. Zhang, and Z. Fang, "Tailoring MoS₂ valley-polarized photoluminescence with super chiral near-field," *Adv. Mater.* **30**, 1801908 (2018).
34. P. K. Jha, N. Shitrit, X. Ren, Y. Wang, and X. Zhang, "Spontaneous exciton valley coherence in transition metal dichalcogenide monolayers interfaced with an anisotropic metasurface," *Phys. Rev. Lett.* **121** (2018).
35. S. Guddala, R. Bushati, M. Li, A. B. Khanikaev, and V. M. Menon, "Valley selective optical control of excitons in 2d semiconductors using a chiral metasurface," *Opt. Mater. Express* **9**, 536 (2019).
36. L. Sun, C.-Y. Wang, A. Krasnok, J. Choi, J. Shi, J. S. Gomez-Diaz, A. Zepeda, S. Gwo, C.-K. Shih, A. Alù, and X. Li, "Separation of valley excitons in a MoS₂ monolayer using a subwavelength asymmetric groove array," *Nat. Photonics* **13**, 180–184 (2019).
37. K. Rong, B. Wang, A. Reuven, E. Maguid, B. Cohn, V. Kleiner, S. Katznelson, E. Koren, and E. Hasman, "Photonic rashba effect from quantum emitters mediated by a berry-phase defective photonic crystal," *Nat. Nanotechnol.* **15**, 927–933 (2020).
38. T. Cao, G. Wang, W. Han, H. Ye, C. Zhu, J. Shi, Q. Niu, P. Tan, E. Wang, B. Liu, and J. Feng, "Valley-selective circular dichroism of monolayer molybdenum disulphide," *Nat. Commun.* **3** (2012).
39. F. Lorén, G. L. Paravicini-Bagliani, S. Saha, J. Gautier, M. Li, C. Genet, and L. Martín-Moreno, "Microscopic analysis of spin-momentum locking on a geometric phase metasurface," *Phys. Rev. B* **107** (2023).
40. L. Martín-Moreno and F. J. García-Vidal, "Minimal model for optical transmission through holey metal films," *J. Physics: Condens. Matter* **20**, 304214 (2008).
41. F. de León-Pérez, G. Brucoli, F. J. García-Vidal, and L. Martín-Moreno, "Theory on the scattering of light and surface plasmon polaritons by arrays of holes and dimples in a metal film," *New J. Phys.* **10**, 105017 (2008).
42. F. J. García-Vidal, L. Martín-Moreno, T. W. Ebbesen, and L. Kuipers, "Light passing through subwavelength apertures," *Rev. Mod. Phys.* **82**, 729–787 (2010).
43. H.-L. Liu, C.-C. Shen, S.-H. Su, C.-L. Hsu, M.-Y. Li, and L.-J. Li, "Optical properties of monolayer transition metal dichalcogenides probed by spectroscopic ellipsometry," *Appl. Phys. Lett.* **105**, 201905 (2014).
44. E. Lorchat, S. Azzini, T. Chervy, T. Taniguchi, K. Watanabe, T. W. Ebbesen, C. Genet, and S. Berciaud, "Room-temperature valley polarization and coherence in transition metal dichalcogenide–graphene van der waals heterostructures," *ACS Photonics* **5**, 5047–5054 (2018).

45. E. Lorchat, L. E. P. López, C. Robert, D. Lagarde, G. Froehlicher, T. Taniguchi, K. Watanabe, X. Marie, and S. Berciaud, “Filtering the photoluminescence spectra of atomically thin semiconductors with graphene,” *Nat. Nanotechnol.* **15**, 283–288 (2020).
46. Y.-J. Chen, J. D. Cain, T. K. Stanev, V. P. Dravid, and N. P. Stern, “Valley-polarized exciton–polaritons in a monolayer semiconductor,” *Nat. Photonics* **11**, 431–435 (2017).
47. S. Dufferwiel, T. P. Lyons, D. D. Solnyshkov, A. A. P. Trichet, A. Catanzaro, F. Withers, G. Malpuech, J. M. Smith, K. S. Novoselov, M. S. Skolnick, D. N. Krizhanovskii, and A. I. Tartakovskii, “Valley coherent exciton-polaritons in a monolayer semiconductor,” *Nat. Commun.* **9** (2018).
48. C. Schneider, M. M. Glazov, T. Korn, S. Höfling, and B. Urbaszek, “Two-dimensional semiconductors in the regime of strong light-matter coupling,” *Nat. Commun.* **9** (2018).
49. J. Sun, H. Hu, D. Pan, S. Zhang, and H. Xu, “Selectively depopulating valley-polarized excitons in monolayer MoS₂ by local chirality in single plasmonic nanocavity,” *Nano Lett.* **20**, 4953–4959 (2020).
50. L. Zheng, Z. Dang, D. Ding, Z. Liu, Y. Dai, J. Lu, and Z. Fang, “Electron-induced chirality-selective routing of valley photons via metallic nanostructure,” *Adv. Mater.* p. 2204908 (2023).
51. T. Gao, M. von Helversen, C. Antón-Solanas, C. Schneider, and T. Heindel, “Atomically-thin single-photon sources for quantum communication,” *npj 2D Mater. Appl.* **7** (2023).